

Enhancement of Gauss–Newton Inversion Method for Biological Tissue Imaging

Majid Ostadrahimi, *Member, IEEE*, Puyan Mojabi, *Member, IEEE*, Amer Zakaria, *Member, IEEE*, Joe LoVetri, *Senior Member, IEEE*, and Lotfollah Shafai, *Life Fellow, IEEE*

Abstract—The multiplicatively regularized Gauss–Newton inversion (GNI) algorithm is enhanced and utilized to obtain complex permittivity profiles of biological objects-of-interest. The microwave scattering data is acquired using a microwave tomography system comprised of 24 co-resident antennas immersed into a saltwater matching fluid. Two types of biological targets are imaged: *ex vivo* bovine legs and *in vivo* human forearms. Four different forms of the GNI algorithm are implemented: a blind inversion, a balanced inversion, a shape-and-location inversion, and a novel balanced shape-and-location inversion. The latter three techniques incorporate typical permittivity values of biological tissues as prior information to enhance the reconstructions. In those images obtained using the balanced shape-and-location reconstruction algorithm, the various parts of the tissue being imaged are clearly distinguishable. The reconstructed permittivity values in the bovine leg images agree with those obtained via direct measurement using a dielectric probe. The reconstructed images of the human forearms qualitatively agree with magnetic resonance imaging images, as well as with the expected dielectric values obtained from the literature.

Index Terms—Animal tissue, Gauss–Newton inversion (GNI), human forearm, imaging, microwave tomography (MWT), shape-and-location reconstruction.

I. INTRODUCTION

MICROWAVE tomography (MWT) has been utilized to retrieve quantitative and qualitative images of various nonbiological objects-of-interest (OIs) in the past, including 3-D [1], and 2-D objects [2], as well as tissue mimicking phantoms [3], [4]. Various experimental prototypes and data acquisition systems have been implemented, such as a single rotary-receiver system [5], a co-resident antenna array [6], and more sophisticated systems based on the modulated scatterer technique and near-field measuring probes [7], [8].

While different biomedical imaging modalities, e.g., X-ray computed tomography (CT), ultrasound, and magnetic resonance imaging (MRI), are standard clinical imaging techniques [9], the use of MWT biomedical imaging is still under investigation. An early tomographic system, developed in the late

1970s [10], used transmission coefficients between two parallel scanning antennas to reconstruct images of a canine kidney [11]. These experiments nurtured plenty of subsequent research on biomedical MWT with various clinical prototypes targeting different applications having been developed. These include systems for the imaging of animal extremities [12], [13], breast cancer diagnosis and detection [4], [14], [15], chemotherapy monitoring [16], calcaneus and heel imaging [17], as well as human forearm imaging [18]. The human forearm is a difficult test case because it contains tissues with a wide range of complex permittivity values. An early human forearm study was reported in [18]. Although scattering data from that study was made available to other researchers to test their inversion algorithms, e.g., [19], no measurements from other MWT systems have been reported.

The mathematical optimization problem associated with quantitative MWT is inherently nonlinear and ill posed. Different algorithms and regularization techniques have been implemented to treat these difficulties; a review of these algorithms is available in [20]. Although the imaging of non-biological objects and dielectric phantoms is essential for quantitative experimentation and the improvement of inversion algorithms, the imaging of real biological tissues provides valuable insight into the performance of MWT for biomedical imaging purposes. Our group has recently completed a pilot study of human forearm imaging that included the collection of MWT scattering data from five volunteers using one of our dipole-based MWT systems. The study also included MRI images of each forearm. Images of each volunteer's forearm were reconstructed in the frequency range from 0.8 to 1.2 GHz. The male and female volunteers were of various ages and the outer adipose layer surrounding the forearm exhibited different thicknesses. It has been our observation that a thicker adipose layer generally makes MWT imaging more difficult, sometimes producing unrecognizable images of the forearm. These observations were based on inversions attempted using both the multiplicatively regularized contrast source inversion (MR-CSI) method, as well as the multiplicatively regularized Gauss–Newton inversion (MR-GNI). Thus, because these are currently state-of-the-art inversion techniques, the dataset is useful as a basis upon which to study improvements to the algorithms that would lead to more robust and accurate imaging with higher resolution.

The general approach taken here is to incorporate expected values of the complex permittivity for the tissues involved in the OI being imaged into the MR-GNI algorithm. With regard to biological tissue imaging, there exist good sources of prior in-

Manuscript received March 07, 2013; revised June 23, 2013; accepted June 25, 2013. Date of publication July 29, 2013; date of current version August 30, 2013. This work was supported by the Natural Sciences and Engineering Research Council (NSERC) of Canada.

The authors are with the Department of Electrical and Computer Engineering, University of Manitoba, Winnipeg, MB, Canada R3T 5V6 (e-mail: Joe_LoVetri@umanitoba.ca).

Color versions of one or more of the figures in this paper are available online at <http://ieeexplore.ieee.org>.

Digital Object Identifier 10.1109/TMTT.2013.2273758

formation in the literature regarding the expected values of relative complex permittivities [21], [22]. The differences in value of the dielectric properties between *in vivo* and *ex vivo* tissues is also well known [23] and could be taken into account. Blind MWT reconstructions of biological targets that neglect available prior information put the already difficult job of inverting the data at a disadvantage resulting in: 1) poor qualitative accuracy, i.e., the different parts of the tissue are not discernible and 2) poor quantitative accuracy, i.e., the obtained complex permittivities may be incorrect. For the case of limb imaging, the inversion problem is especially difficult because of the wide range of complex permittivity values associated with the tissues involved: skin, adipose, muscle, and bone. In addition to the ill-posed nonlinear characteristics of the mathematical problem and the wide variety of tissues involved, MWT tissue imaging is also difficult because of the large difference between the real and imaginary parts of the permittivity. That is, MWT algorithms may favor either the real or the imaginary part of the reconstruction [24]. These difficulties are also compounded by the fact that most numerical algorithms do not fully model the complete MWT experimental system where the measurements are made. This leads to modeling error, which is the mismatch between the numerical model being used in the inversion algorithm and the experimental system.

In this paper, we investigate the use of prior information in the form of estimated complex permittivity values for the various tissues as a means of improving the imaging performance of MR-GNI [25]. For this study, four different implementations of MR-GNI are utilized with or without the use of prior information. The OIs being imaged are *ex vivo* animal tissues: two bovine legs with and without skin, and *in vivo* human forearms: two volunteers one with a thin and another with a thick adipose layer. The former objects, *ex vivo* targets, are used for quantitative evaluation because their dielectric properties can also be measured using a dielectric probe. The *in vivo* human forearms are used for qualitative evaluation because the MRI image of the volunteers are also available. We first present *blind* reconstructions without the use of any prior information (Section IV-A). We then present the results obtained by balancing the real and imaginary parts of the image (Section IV-B), as well as shape-and-location reconstruction of the tissues (Section IV-C). Finally, we reconstruct the images of each tissue using a novel combination of the shape-and-location and balanced MR-GNI (Section IV-D). From the results obtained (presented in Section VI), the use of balanced shape-and-location reconstruction enhances the quality of the images where different parts of the tissue are clearly distinguished. We also measured the permittivity of the bovine legs using a commercial dielectric probe (Section V) and found that the complex permittivity values for the different tissue regions agree with the direct dielectric probe measurements.

II. SYSTEM DESCRIPTION

The measurement system consists of a metallic enclosure comprising 24 dipole antennas designed for operation at 1 GHz in the water matching medium. The antennas are held by rigid coaxial cables that feed through to a vector network analyzer

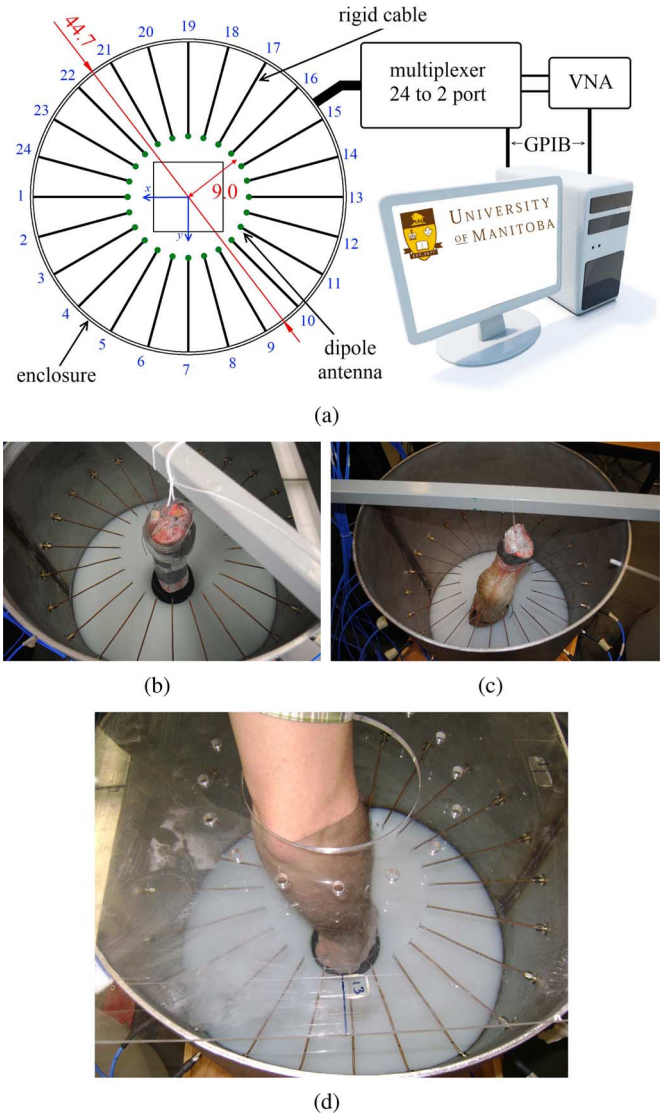


Fig. 1. Measurement system. (a) Schematic diagram (dimensions in centimeters). (b) Photograph during measurement of a skinless bovine leg. (c) Bovine leg with skin. (d) Photograph during measurement of a volunteer's forearm.

(VNA) that collects the scattering parameter, S_{21} , between each pair of the antennas. The two ports of the VNA connect to the antennas via a 24-2 port multiplexer. The VNA and multiplexer are controlled through a general purpose interface bus (GPIB) using a custom designed data acquisition program. A schematic diagram of the system is shown in Fig. 1(a). Photographs of the system during measurements are shown in Fig. 1(b)–(d).

A. Matching Fluid

A matching fluid consisting of simple table salt in deionized water was used to decrease the dielectric contrast between the OI and the background medium. Saltwater was used because it is readily available, inexpensive, and comfortable, as well as nontoxic for the volunteers. Its matching performance is good for high-permittivity tissues such as skin and muscle. The high dielectric constant increases the amount of energy that couples into the OI while the introduction of loss (i.e., conductivity) ensures that reflected waves from the boundary will be sufficiently attenuated to make image reconstruction possible

TABLE I
MATCHING FLUID RELATIVE COMPLEX
PERMITTIVITY ($\epsilon_b = \epsilon'_r - \epsilon''_r$)

Solution	at 0.8 GHz	at 1.2 GHz
Salt_12.5	76 - j14	76 - j11
Salt_15	77 - j17	76 - j14

using only a simple model of the system. A lossless matching fluid would have required a more complicated system model that accounts for the multiple wave reflections from the boundaries, as well as the mutual coupling between the coexistent antennas. Without such a model, the image reconstruction would be poor due to the large modeling error. Our group has studied the effects of varying the matching fluid's loss by changing the amount of salt that was added to the water [26]. The resulting imaginary part of the permittivity was so varied from $|\text{Im}(\epsilon_b)| = 4$ up to $|\text{Im}(\epsilon_b)| = 25$ at 1 GHz. Imaging results for a cylindrical phantom consisting of a glycerol/deionized water solution were compared using single frequency reconstructions in the frequency range from 0.8 to 1.2 GHz. The worst reconstructions were obtained with matching fluids of $|\text{Im}(\epsilon_b)| = 4$ (lossless) and $|\text{Im}(\epsilon_b)| = 25$ (high loss). It was shown that a broad range of loss can be used for imaging and the best results were obtained with $|\text{Im}(\epsilon_b)| = 12.5$ and $|\text{Im}(\epsilon_b)| = 15.0$ at 1 GHz. In this paper, we refer to these solutions as salt_12.5 and salt_15, respectively. Salt_12.5 requires 2.5 g/L of table salt and salt_15 requires 3.14 g/L. A commercially available dielectric probe was used to measure the complex dielectric properties of the matching fluid. The measured permittivities of the matching fluids are listed in Table I.

III. PROBLEM STATEMENT

The goal is to reconstruct the complex dielectric properties of an OI, denoted by $\epsilon_r(\mathbf{r})$, at positions \mathbf{r} within a square imaging domain \mathcal{D} located inside the measurement enclosure. The measurement domain, \mathcal{S} , consists of a set of points encircling \mathcal{D} at which the antennas are located [see Fig. 1(a)]. Both imaging and measurement domains are immersed in a background medium with relative complex permittivity ϵ_b . In our case, the background medium is one of the previously described saltwater solutions. The inversion problem is formulated in terms of an unknown contrast function defined as

$$\chi(\mathbf{r}) \triangleq \frac{\epsilon_r(\mathbf{r}) - \epsilon_b}{\epsilon_b}. \quad (1)$$

The objective is to find $\chi(\mathbf{r} \in \mathcal{D})$ from calibrated scattered electric-field measurements, $E_{\text{cal}}^{\text{sct}}(\mathbf{r} \in \mathcal{S})$. We assume a 2-D transverse-magnetic (TM) illumination where the electric field can be represented by a single component perpendicular to the imaging domain (the z -component).

Raw scattered field measurements, $E_{\text{meas}}^{\text{sct}}$, are obtained by performing two different sets of measurements. First, the OI is successively illuminated by each transmitter and the resulting fields are collected by the receivers. We refer to this set of measurements as the total-field data, $E_{\text{meas}}^{\text{tot}}$. Second, the same experiment is performed in the absence of the OI. This set of measure-

ments is referred to as the incident-field data, $E_{\text{meas}}^{\text{inc}}$. The *measured* scattered-field data, $E_{\text{meas}}^{\text{sct}}$, is then obtained by subtracting the incident-field from the total-field data. This measured scattered-field data is first calibrated before it is submitted to the inversion algorithm. Calibration is used to convert the raw experimental data to what would be expected in the assumed numerical model and thereby reduce the modeling error. Various calibration methods, based on the expected incident field and scattered field for known targets, have been reported [27]. Herein we employ the so-called scattered-field calibration method exclusively. In this method, the raw $E_{\text{meas}}^{\text{sct}}$ is calibrated by multiplying it with a factor determined as the ratio of the analytically derived scattered field to the measured scattered field for a known perfect electric conductor (PEC) calibration cylinder (In this study the diameter of the PEC cylinder is 3.5 in). That is, the calibrated measured scattered-field data due to the OI, $E_{\text{cal}}^{\text{sct}}$, is obtained as

$$E_{\text{cal}}^{\text{sct}} = \text{cal} \times E_{\text{meas}}^{\text{sct}} \quad (2)$$

where the calibration factor cal is given by

$$\text{cal} = \frac{\text{analytical scattered data due to the PEC cylinder}}{\text{measured scattered data due to the PEC cylinder}}. \quad (3)$$

The contrast function is discretized into N square pixels and represented by $\underline{\chi}$, a complex vector of length N . The calibrated measured scattered-field data is also represented by a complex vector, $\underline{E}_{\text{cal}}^{\text{sct}}$, of length M where M is the product of the number of transmitter and receiver antennas. Denoting $\underline{E}^{\text{sct}}(\underline{\chi})$ as the simulated scattered field on \mathcal{S} due to a predicted contrast $\underline{\chi}$, the MWT problem is formulated as the minimization of the following data misfit cost-functional:

$$\mathcal{C}^{LS}(\underline{\chi}) = \eta_S \left\| \underline{E}^{\text{sct}}(\underline{\chi}) - \underline{E}_{\text{cal}}^{\text{sct}} \right\|_{\mathcal{S}}^2 \quad (4)$$

where $\| \cdot \|_{\mathcal{S}}$ denotes the L_2 -norm on \mathcal{S} . The weighting coefficient η_S is chosen to be

$$\eta_S = \left\| \underline{E}_{\text{cal}}^{\text{sct}} \right\|_{\mathcal{S}}^{-2}. \quad (5)$$

IV. INVERSION ALGORITHMS

To minimize the nonlinear ill-posed cost-functional $\mathcal{C}^{LS}(\underline{\chi})$, we use four different forms of the GNI algorithm. The first one is a *blind* inversion algorithm that does not assume any prior information about the OI. The second one is a balanced inversion algorithm that assumes that an approximate ratio between the average real and imaginary parts of the contrast is known. The third one is a shape-and-location reconstruction algorithm that assumes that approximate values of the contrast values are known. The last one is a balanced shape-and-location reconstruction algorithm that can handle both the numerical imbalance between the real and imaginary parts of the contrast values and assumes approximate values of the contrast.

A. Blind Inversion

For the blind inversion, we utilize the MR-GNI algorithm. This inversion algorithm utilizes the so-called weighted

L_2 -norm total variation multiplicative regularizer in conjunction with the GNI method. At the n th iteration of the MR-GNI algorithm, the following cost-functional is constructed:

$$\mathcal{C}_n^{\text{blind}}(\underline{\chi}) = \mathcal{C}^{LS}(\underline{\chi})\mathcal{C}_n^{MR}(\underline{\chi}). \quad (6)$$

The multiplicative regularizer, \mathcal{C}_n^{MR} (in the continuous domain), is given as

$$\mathcal{C}_n^{MR}(\chi) = \frac{1}{A} \int_{\mathcal{D}} \frac{|\nabla\chi(\mathbf{r})|^2 + \delta_n^2}{|\nabla\chi_n(\mathbf{r})|^2 + \delta_n^2} d\mathbf{r} \quad (7)$$

where the gradient ∇ is taken with respect to the position vector \mathbf{r} , and A is the area of the imaging domain. The steering parameter δ_n^2 is chosen to be [2], [25]

$$\delta_n^2 = \frac{\mathcal{C}^{LS}(\underline{\chi}_n)}{\Delta A} \quad (8)$$

where ΔA is the area of a single cell in the uniformly discretized domain \mathcal{D} . In the MR-GNI algorithms, the contrast is updated in the form of $\underline{\chi}_{n+1} = \underline{\chi}_n + \nu_n \Delta \underline{\chi}_n$, where ν_n is the step-length determined via an appropriate line search algorithm. The correction $\Delta \underline{\chi}_n$ is found by solving the following equation:

$$(\underline{\mathbf{J}}_n^H \underline{\mathbf{J}}_n + \beta_n \underline{\mathbf{L}}_n) \Delta \underline{\chi}_n = -\underline{\mathbf{J}}_n^H \underline{\mathbf{d}}_n - \beta_n \underline{\mathbf{L}}_n \underline{\chi}_n \quad (9)$$

where $\underline{\mathbf{J}}_n \in \mathbb{C}^{M \times N}$ is the Jacobian matrix. The discrepancy vector $\underline{\mathbf{d}}_n$ is given as

$$\underline{\mathbf{d}}_n = \underline{\mathbf{E}}^{\text{sct}}(\underline{\chi}_n) - \underline{\mathbf{E}}^{\text{cal}}. \quad (10)$$

and $\beta_n = \|\underline{\mathbf{d}}_n\|^2$. The regularization operator $\underline{\mathbf{L}}_n$ represents the discrete form of the operator “ $-\nabla \cdot b_n^2 \nabla$ ” where “ $\nabla \cdot$ ” is the divergence operator and

$$b_n^2(\mathbf{r}) = A^{-1} (|\nabla\chi_n(\mathbf{r})|^2 + \delta_n^2)^{-1}. \quad (11)$$

This completes the brief description of the basic MR-GNI algorithm.

B. Balanced Inversion

Due to the imbalance between the average values of the real and imaginary parts of the relative complex permittivity of biological tissues, it is likely that a blind inversion algorithm favors the reconstruction of the real part. This imbalance reconstruction can be alleviated by adjusting the regularization weight for the real and imaginary parts of the contrast. In the balanced GNI algorithm, it is assumed that the average real part of the contrast is Q times greater than the imaginary part of the contrast. Therefore, this approximate ratio, Q , serves as the prior information. Thus, in the balanced MR-GNI, the following data misfit cost-functional is minimized at the n th iteration of the algorithm:

$$\mathcal{C}_n^{\text{balanced}}(\underline{\chi}) = \mathcal{C}^{LS}(\underline{\chi})\mathcal{C}_n^{\text{PSMR}}(\underline{\chi}) \quad (12)$$

where the balanced MR (in the continuous domain) is given as

$$\mathcal{C}_n^{\text{PSMR}}(\chi) = \int_{\mathcal{D}} (b_n^{\text{PS}})^2 (|\nabla\chi_R|^2 + Q^2|\nabla\chi_I|^2 + \delta_n^2) d\mathbf{r} \quad (13)$$

and χ_R and χ_I are the real and imaginary parts of the contrast χ , respectively. The weighting b_n^{PS} is given as

$$b_n^{\text{PS}}(\mathbf{r}) = A^{-\frac{1}{2}} (|\nabla\chi_{R,n}(\mathbf{r})|^2 + Q^2|\nabla\chi_{I,n}(\mathbf{r})|^2 + \delta_n^2)^{-\frac{1}{2}}. \quad (14)$$

Also, $\chi_{R,n}$ and $\chi_{I,n}$ are the real and imaginary parts of the predicted contrast at the n th iteration of the GNI algorithm. As can be seen, the weight of $|\nabla\chi_I|$ is chosen to be Q times more than that of $|\nabla\chi_R|$ so as to balance the contribution of these two quantities in the multiplicative regularizer. We note that when Q is chosen to be 1, $\mathcal{C}_n^{\text{PSMR}}$ will be the same as $\mathcal{C}_n^{\text{MR}}$ given in (7).

As has been shown in [24], the real and imaginary parts of the contrast are updated as $\underline{\chi}_{R,n+1} = \underline{\chi}_{R,n} + \nu_n Q \Delta \underline{\chi}_{R,n}^{\text{PS}}$ and $\underline{\chi}_{I,n+1} = \underline{\chi}_{I,n} + \nu_n \Delta \underline{\chi}_{I,n}^{\text{PS}}$, where the corrections $\Delta \underline{\chi}_{R,n}^{\text{PS}}$ and $\Delta \underline{\chi}_{I,n}^{\text{PS}}$ can be found by solving the following equation:

$$\underline{\mathbf{H}}_{\text{GN},n}^{\text{PS}} \begin{bmatrix} \Delta \underline{\chi}_{R,n}^{\text{PS}} \\ \Delta \underline{\chi}_{I,n}^{\text{PS}} \end{bmatrix} = -\underline{\mathbf{g}}_n^{\text{PS}}. \quad (15)$$

As shown in [24], the pre-scaled gradient vector $\underline{\mathbf{g}}_n^{\text{PS}}$ can be conveniently written as

$$2\eta_S \begin{bmatrix} Q \text{Re}(\underline{\mathbf{J}}_n^H \underline{\mathbf{d}}_n) + Q\beta_n \underline{\mathbf{L}}_n^{\text{PS}} \underline{\chi}_{R,n} \\ \text{Im}(\underline{\mathbf{J}}_n^H \underline{\mathbf{d}}_n) + Q^2\beta_n \underline{\mathbf{L}}_n^{\text{PS}} \underline{\chi}_{I,n} \end{bmatrix} \quad (16)$$

and the matrix $\underline{\mathbf{H}}_{\text{GN},n}^{\text{PS}}$ as

$$2\eta_S \begin{bmatrix} Q^2 \text{Re}(\underline{\mathbf{J}}_n^H \underline{\mathbf{J}}_n) + Q^2\beta_n \underline{\mathbf{L}}_n^{\text{PS}} & -Q \text{Im}(\underline{\mathbf{J}}_n^H \underline{\mathbf{J}}_n) \\ Q \text{Im}(\underline{\mathbf{J}}_n^H \underline{\mathbf{J}}_n) & \text{Re}(\underline{\mathbf{J}}_n^H \underline{\mathbf{J}}_n) + Q^2\beta_n \underline{\mathbf{L}}_n^{\text{PS}} \end{bmatrix}. \quad (17)$$

The operator $\underline{\mathbf{L}}_n^{\text{PS}}$ is the discrete form of the operator “ $-\nabla \cdot (b_n^{\text{PS}})^2 \nabla$ ” [24].

C. Shape-and-Location Inversion

Assume that the imaging domain \mathcal{D} consists of L contrast values; each of which has a known contrast of $\chi_\ell^h \in \mathbb{C}$, where $\ell = 1, \dots, L$. Here, the goal is to find the spatial distribution (shape-and-location) of these contrast values. To this end, we construct the regularized cost-functional $\mathcal{C}_n^{\text{shape}}(\chi)$ at the n th iteration of the inversion algorithm as [28]

$$\mathcal{C}_n^{\text{shape}}(\chi) = \mathcal{C}^{LS}(\chi)\mathcal{C}_n^{\text{hom}}(\chi)\mathcal{C}_n^{\text{MR}}(\chi) \quad (18)$$

where

$$\mathcal{C}_n^{\text{hom}}(\chi) = \frac{1}{A} \int_{\mathcal{D}} \prod_{\ell=1}^L \frac{|\chi(\mathbf{r}) - \chi_\ell^h|^2 + \alpha_n^2}{|\chi_n(\mathbf{r}) - \chi_\ell^h|^2 + \alpha_n^2} d\mathbf{r}. \quad (19)$$

The steering parameter α_n is chosen to be

$$\alpha_n^2 = \mathcal{C}^{LS}(\chi_n). \quad (20)$$

In this method, the contrast is updated as $\underline{\chi}_{n+1} = \underline{\chi}_n + \nu_n \Delta \underline{\chi}_n$ where the correction is found by solving the following equation:

$$\begin{aligned} & \left(\mathbf{J}_n^H \mathbf{J}_n + \beta_n \underline{\mathbf{L}}_n + \beta_n \sum_{\ell=1}^L \underline{\mathbf{D}}_{\ell,n} \right) \Delta \underline{\chi}_n \\ & = -\mathbf{J}_n^H \underline{\mathbf{d}}_n - \beta_n \underline{\mathbf{L}}_n \underline{\chi}_n - \beta_n \sum_{\ell=1}^L \underline{\mathbf{D}}_{\ell,n} (\underline{\chi}_n - \chi_\ell^h \underline{\mathbf{e}}) \end{aligned} \quad (21)$$

where $\underline{\mathbf{e}} \in \mathbb{R}^N$ is a vector of all ones. The matrix $\underline{\mathbf{D}}_{\ell,n} \in \mathbb{R}^{N \times N}$ is a diagonal matrix given as

$$\underline{\mathbf{D}}_{\ell,n} = \text{diag} \left(\frac{1}{A} \xi_{\ell,n}^2 \right) \quad (22)$$

where $\xi_{\ell,n}^2 \in \mathbb{R}^N$ is the discretized form of

$$\xi_{\ell,n}^2(\mathbf{r}) = (|\chi_n(\mathbf{r}) - \chi_\ell^h|^2 + \alpha_n^2)^{-1}. \quad (23)$$

D. Balanced Shape-and-Location Inversion

If there is an imbalance between the average values of the real and imaginary parts of the contrast, the shape-and-location reconstruction may favor one. Therefore, in this paper, we introduce a balanced shape-and-location reconstruction algorithm, which can alleviate this problem. In the proposed balanced shape-and-location reconstruction, we minimize the following cost-functional

$$c_n^{\text{Balanced-shape}}(\chi) = c^{\text{LS}}(\chi) c_n^{\text{hom}}(\chi) c_n^{\text{PSMR}}(\chi). \quad (24)$$

The real and imaginary parts of the contrast are updated as $\underline{\chi}_{R,n+1} = \underline{\chi}_{R,n} + \nu_n Q \Delta \underline{\chi}_{R,n}^{\text{PS}}$ and $\underline{\chi}_{I,n+1} = \underline{\chi}_{I,n} + \nu_n \Delta \underline{\chi}_{I,n}$, where the corrections $\Delta \underline{\chi}_{R,n}^{\text{PS}}$ and $\Delta \underline{\chi}_{I,n}$ can be found by solving the following equation:

$$\underline{\mathbf{H}}_{\text{GN},n}^{\text{PS-shape}} \begin{bmatrix} \Delta \underline{\chi}_{R,n}^{\text{PS}} \\ \Delta \underline{\chi}_{I,n} \end{bmatrix} = -\underline{\mathbf{g}}_n^{\text{PS-shape}}. \quad (25)$$

By finding the first derivatives of the cost-functional, the pre-scaled gradient vector $\underline{\mathbf{g}}_n^{\text{PS-shape}}$ can be conveniently written as

$$\underline{\mathbf{g}}_n^{\text{PS}} + 2\eta_S \begin{bmatrix} Q\beta_n \sum_{\ell=1}^L \underline{\mathbf{D}}_{\ell,n} \text{Re}(\underline{\chi}_n - \chi_\ell^h \underline{\mathbf{e}}) \\ \beta_n \sum_{\ell=1}^L \underline{\mathbf{D}}_{\ell,n} \text{Im}(\underline{\chi}_n - \chi_\ell^h \underline{\mathbf{e}}) \end{bmatrix} \quad (26)$$

and by finding the second derivatives of the cost-functional, the matrix $\underline{\mathbf{H}}_{\text{GN},n}^{\text{PS-shape}}$ as

$$\underline{\mathbf{H}}_{\text{GN},n}^{\text{PS}} + 2\eta_S \begin{bmatrix} Q^2 \beta_n \sum_{\ell=1}^L \underline{\mathbf{D}}_{\ell,n} & \mathbf{0} \\ \mathbf{0} & \beta_n \sum_{\ell=1}^L \underline{\mathbf{D}}_{\ell,n} \end{bmatrix}. \quad (27)$$

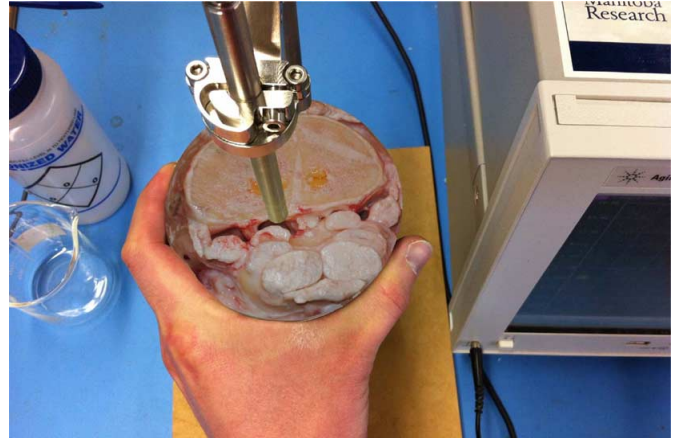


Fig. 2. Photograph of a bovine leg imaging plane during direct permittivity measurement using a dielectric probe.

V. OIs

Using these four versions of the MR-GNI algorithm, the complex dielectric properties of three different OIs are reconstructed: 1) an excised bovine leg with its skin removed; 2) a bovine leg with skin intact; and 3) two human forearms from two different volunteers, one with a thin layer of adipose tissue and one with a thick layer of adipose tissue.

The dielectric properties of the bovine leg tissues were measured directly using a dielectric probe. The direct dielectric measurement enables us to validate the quantitative accuracy of the reconstructed images. We refer to the bovine leg imaging as the *ex vivo* imaging. These direct dielectric probe measurements were performed immediately after the MWT data was collected by cutting the bovine legs in half at the location of the imaging plane. A photograph of the probe is shown in Fig. 2.

A schematic of the anatomy and a photograph of a bovine leg are shown in Fig. 3(a) and (b). This anatomy consists of many tiny veins and structures. For an accurate dielectric measurement, our probe requires access to a minimum cross section of 5 mm, thus we could only measure the permittivity of the skin, bone, and flexor. The results are presented in Table II. The *in vivo* experiments included the imaging of the human forearms (left or right) of five volunteers who participated under a University of Manitoba Biomedical Research Ethics Board approved protocol. The forearm data were collected using the system shown in Fig. 1 where each volunteer held their arm inside the measurement enclosure parallel to the z -axis [see Fig. 1(d)]. The volunteers were able to remain stationary during the data collection, approximately 1 min, by resting their upper arm on the Plexiglas plate, which was placed on top of the chamber.

Here, images for only two of the volunteers are presented. Volunteer #1 has a thin layer of adipose tissue, whereas volunteer #4 has a thick layer of adipose tissue. These represent the two extremes found in our subjects. Each volunteer's forearm was imaged using a 0.2-T E-scan MRI, with a forearm coil, immediately after the MWT data was collected. In order to identify the MWT imaging plane in the 3-D MRI image, during the MRI scan a vitamin E capsule was attached to each volunteer's forearm at the location of the MWT imaging plane. This capsule

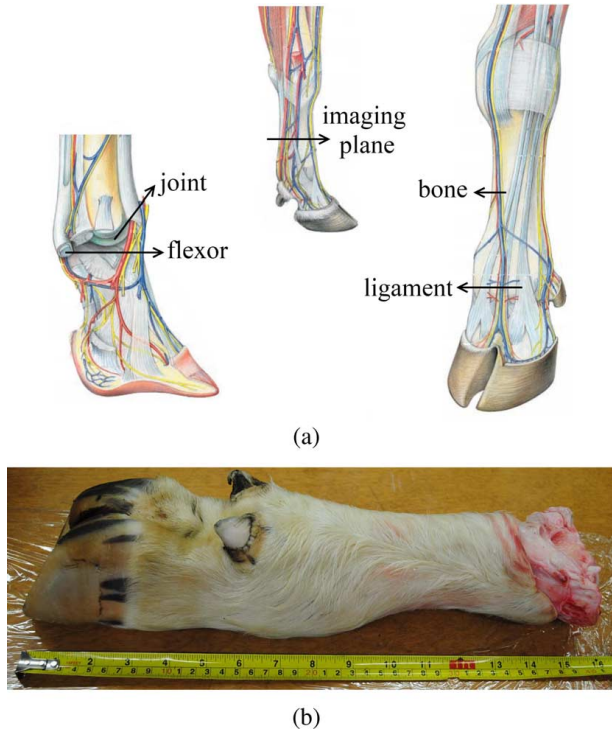


Fig. 3. (a) Anatomy of a bovine leg reproduced with permission from [29, pp. 5, 9, 11]. (b) Photograph of a bovine leg used for imaging.

TABLE II
MEASURED RELATIVE COMPLEX PERMITTIVITY
OF BOVINE LEG

	0.8 GHz	1.0 GHz	1.2 GHz
bone	26 - j8	25 - j7	25 - j7
flexor	54 - j18	53 - j16	53 - j15
skin	64 - j20	63 - j18	63 - j16

is clearly visible in the MRI images. During the MRI scan, the volunteers were in supine position, resting their forearms on a bed. Thus, the orientation of the arm during the MRI scan was different than during the MWT data collection. The purpose of the MRI image is to enable us to qualitatively validate our MWT images.

VI. IMAGING RESULTS

In this section, the reconstructed real and imaginary parts of the permittivity of each OI is presented. The data for each OI was collected in the frequency range from 0.4 to 1.4 GHz in 0.1-GHz steps. The best images were obtained at frequencies in the range from 0.8 to 1.2 GHz with either matching fluid, salt_12.5 or salt_15. For each OI, we present the results from a blind inversion (Section IV-A), balanced inversion (Section IV-B), shape-and-location reconstruction (Section IV-C), and balanced shape-and-location reconstruction (Section IV-D).

The balancing factor Q was set to 10 for the balanced reconstructions. Q is usually calculated approximately as the ratio of the average value of the real to imaginary parts of the contrast value of the object. Changing the Q factor about the average value may improve the imaging performance [24].

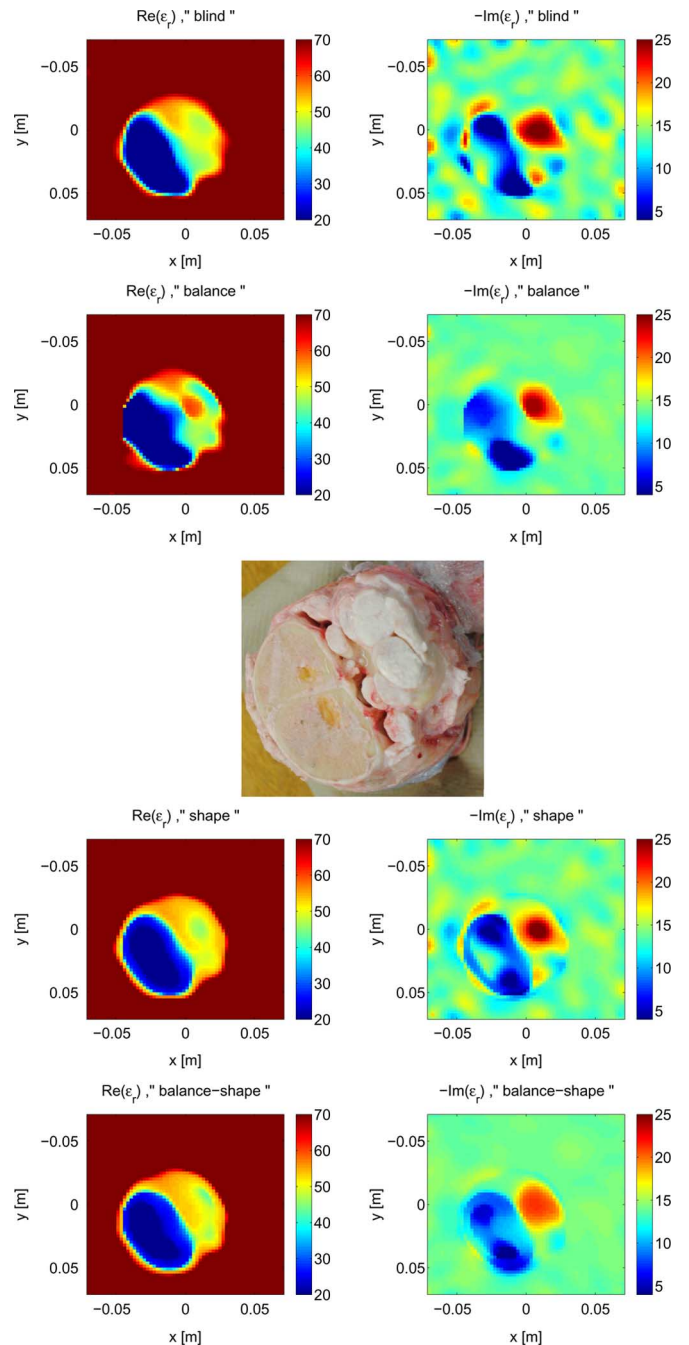


Fig. 4. Images of $\text{Re}(\epsilon_r)$ (left) and $\text{Im}(\epsilon_r)$ (right) of the skinless bovine leg, matching fluid: salt_12.5, frequency of 0.8 GHz. First row: blind inversion, second row: balanced inversion, third row: photograph of the imaging plane, fourth row: shape-and-location inversion, and fifth row: balanced shape-and-location inversion.

For the shape-and-location reconstructions, the algorithm requires some prior information about the permittivities of the object, as discussed in Sections IV-C and IV-D. Here, the L -parameter is set to 3, which means three permittivity values were given to the algorithm. Note that we have already studied the effect of the number of contrast values on the image quality. Providing more contrast values usually improves the imaging results [28]. In the bovine leg experiment, the three permittivities are: 1) background medium; 2) bone; and 3) flexor. In the forearm experiment, the three permittivities are: 1) background medium; 2) bone; and 3) muscle. One way of supplying the

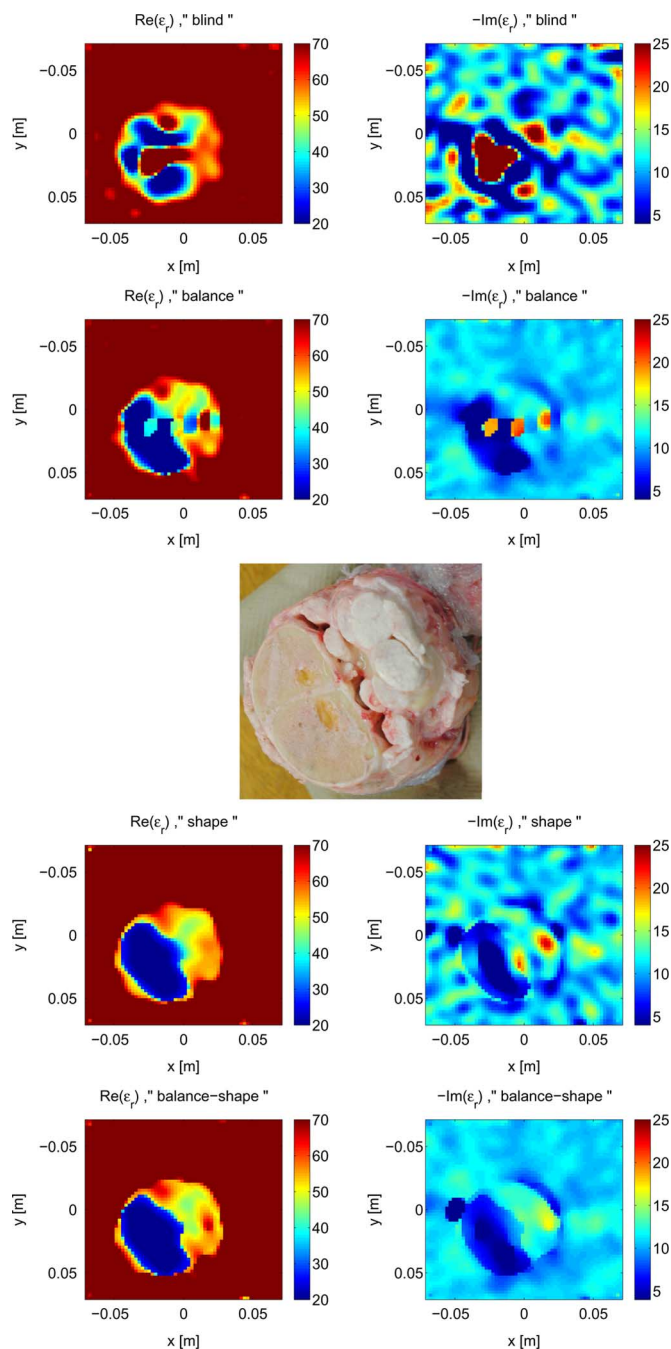


Fig. 5. Images of $\text{Re}(\epsilon_r)$ (left) and $\text{Im}(\epsilon_r)$ (right) of the skinless bovine leg, matching fluid: salt_12.5, frequency of 1.2 GHz. First row: blind inversion, second row: balanced inversion, third row: photograph of the imaging plane, fourth row: shape-and-location inversion, and fifth row: balanced shape-and-location inversion.

known permittivities to the algorithm is to obtain them from the literature. For instance, the permittivities of bone and muscle are available in [21]. The other way to extract the prior permittivity information is using the blind reconstruction. In this paper, we used the latter method, using the blindly reconstructed images. For each tissue, such as bone, a point within the tissue region was randomly selected and its permittivity was then given to the shape-and-location algorithm. Note that different point locations provide different permittivity values. We tried different locations and the obtained images were similar, thus the

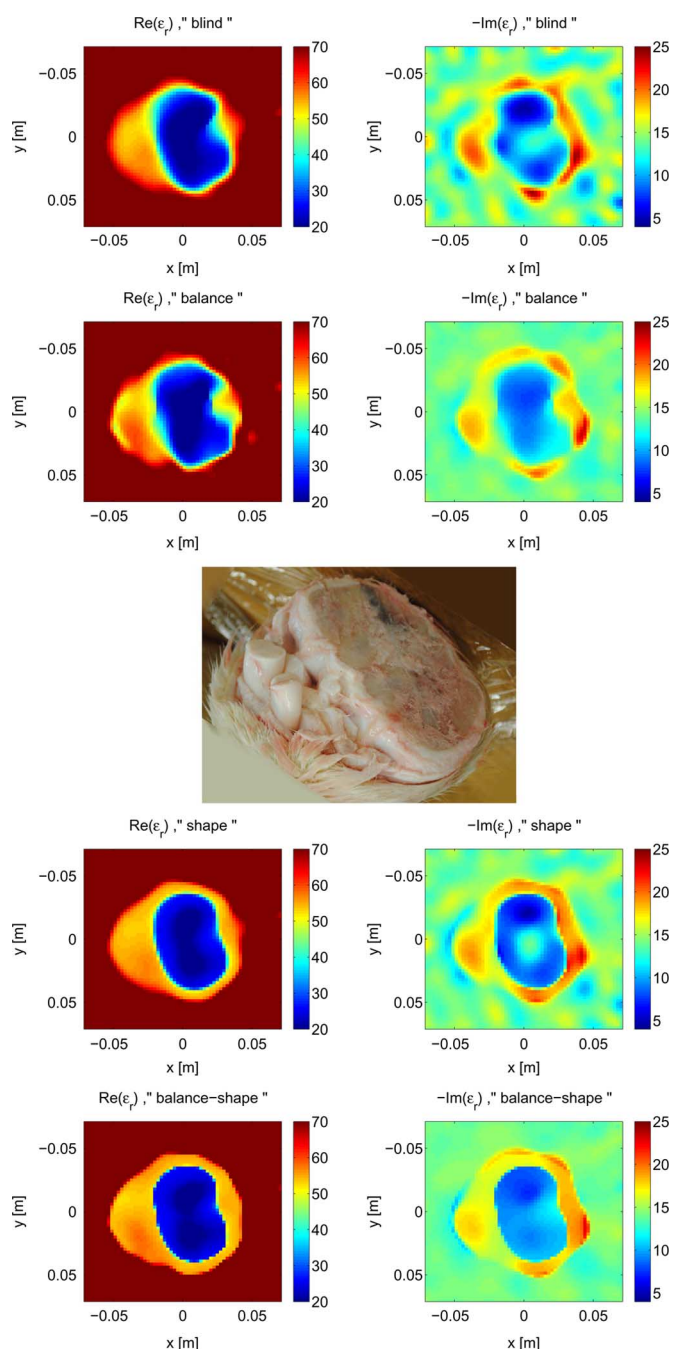


Fig. 6. Images of $\text{Re}(\epsilon_r)$ (left) and $\text{Im}(\epsilon_r)$ (right) of the bovine leg, matching fluid: salt_12.5, frequency of 0.8 GHz. First row: blind inversion, second row: balanced inversion, third row: a photograph of the imaging plane, fourth row: shape-and-location inversion, and fifth row: balanced shape-and-location inversion.

shape-and-location reconstruction is not very sensitive to these values.

A. Skinless Bovine Leg

The imaging results of the skinless bovine leg at frequencies of 0.8 and 1.2 GHz are shown in Figs. 4 and 5, respectively. A photograph of the cross section at the imaging plane is also presented. Note that the imaging domain length is set to 15 cm due to a relatively large sizes of the leg. Moreover, during plotting of the real part of the images, the upper color limit was set to

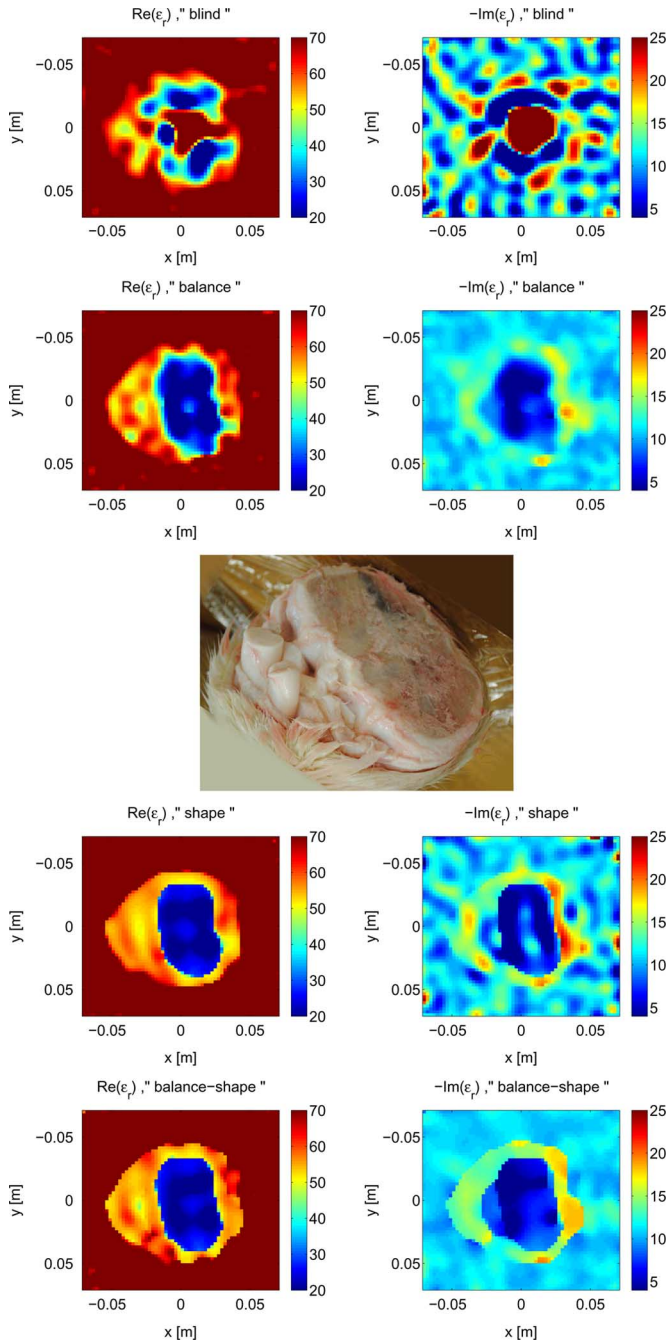


Fig. 7. Images of $\text{Re}(\epsilon_r)$ (left) and $\text{Im}(\epsilon_r)$ (right) of the bovine leg, matching fluid: salt_12.5, frequency of 1.2 GHz. First row: blind inversion, second row: balanced inversion, third row: a photograph of the imaging plane, fourth row: shape-and-location inversion, and fifth row: balanced shape-and-location inversion.

70, which is less than that of the real permittivity of the background matching fluid [≈ 76 (see Table I)]. The upper limit of 70 creates a uniform image background and is only applied for displaying purposes.

Note that the modeling error is higher at 1.2 GHz than at 0.8 GHz because of the poorer performance of the dipole antennas. The images obtained from blind inversions at 1.2 GHz (Fig. 5) contain more artifacts and noise than those obtained at 0.8 GHz (Fig. 4). We present the imaging results at both frequencies to show that enhancement of the images is possible from

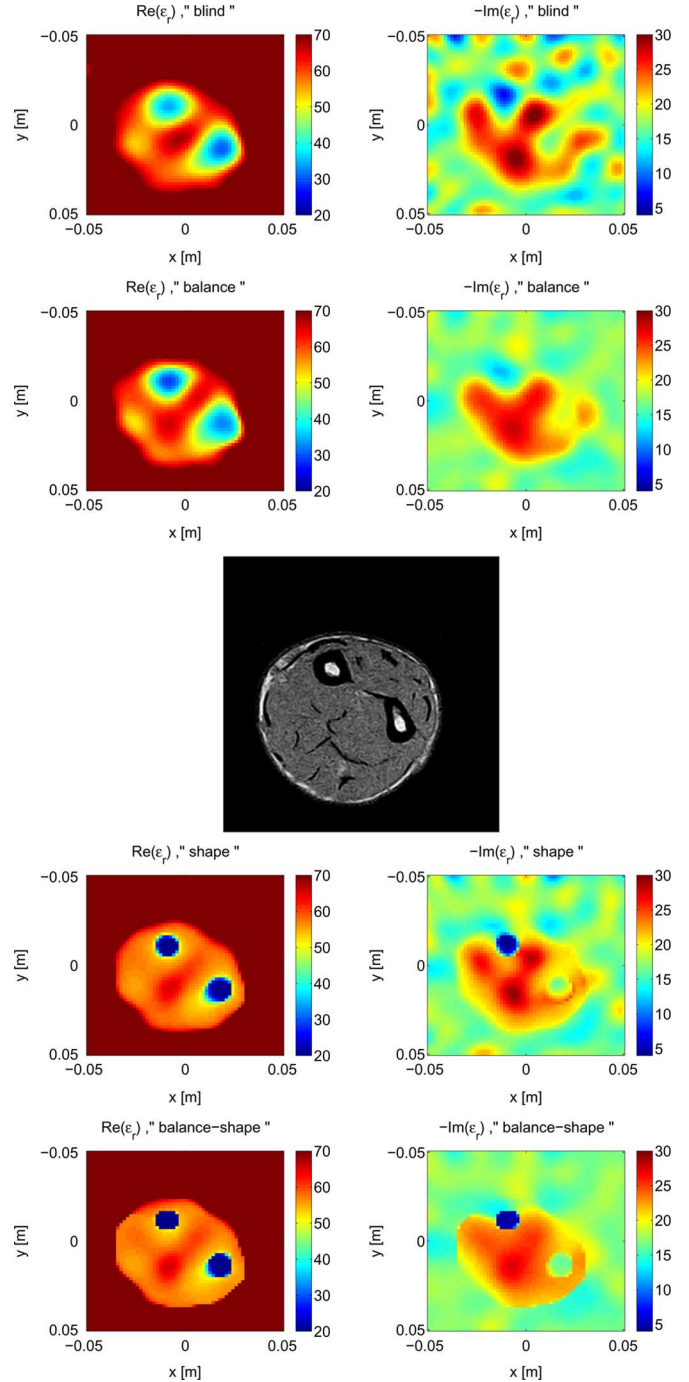


Fig. 8. Images of $\text{Re}(\epsilon_r)$ (left) and $\text{Im}(\epsilon_r)$ (right) of volunteer 1's forearm, matching fluid: salt_15, frequency of 0.8 GHz. First row: blind inversion, second row: balanced inversion, third row: MRI image at the imaging plane, fourth row: shape-and-location inversion, and fifth row: balanced shape-and-location inversion.

lower quality data, at 1.2 GHz, as well as from higher quality data, at 0.8 GHz.

B. Bovine Leg

Similar to the skinless bovine leg, reconstructed images of a bovine leg with skin at frequencies of 0.8 and 1.2 GHz are shown in Figs. 6 and 7, respectively. The reconstructed real and imaginary parts of the permittivity agree with the measured permittivities in Table II. As for the skinless case, the imaging domain size is 15 cm.

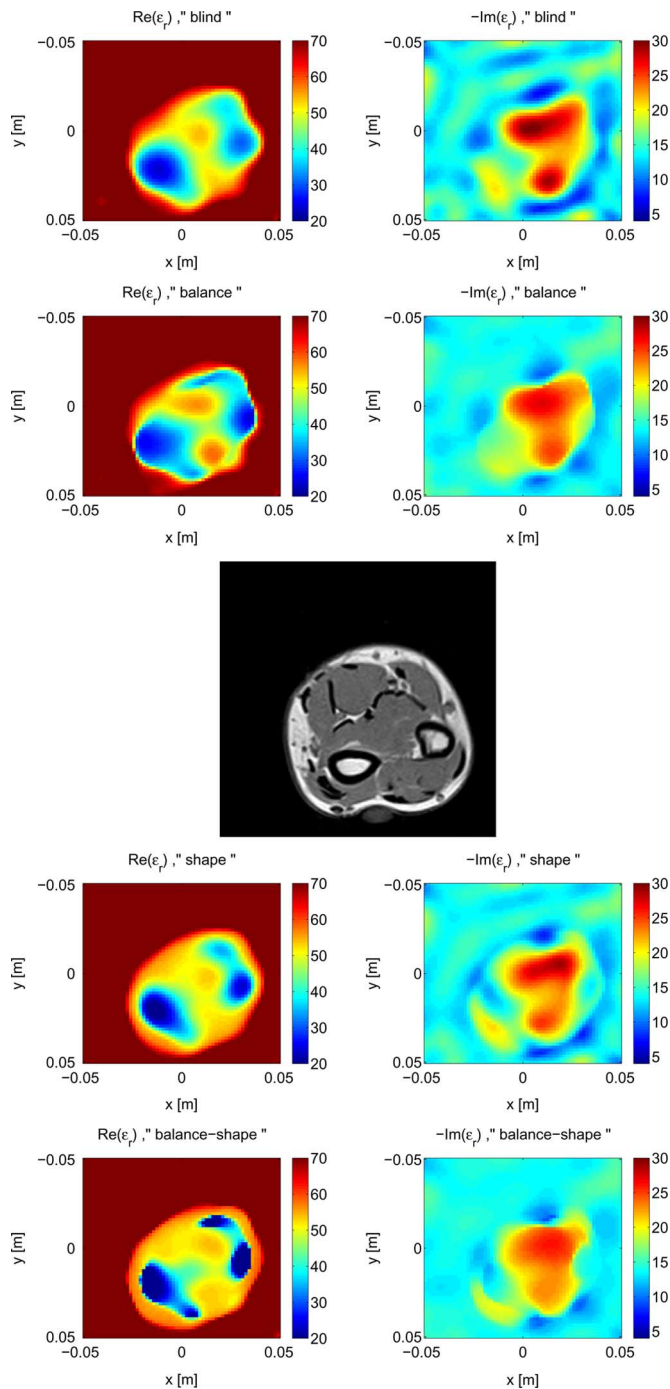


Fig. 9. Images of $\text{Re}(\epsilon_r)$ (left) and $\text{Im}(\epsilon_r)$ (right) of volunteer 4's forearm, matching fluid: salt_12.5, frequency of 0.8 GHz. First row: blind inversion, second row: balanced inversion, third row: MRI image at the imaging plane, fourth row: shape-and-location inversion, and fifth row: balanced shape-and-location inversion.

Again the modeling error is higher at 1.2 GHz than 0.8 GHz. Thus, the images obtained from a blind inversion at 1.2 GHz (Fig. 7) contain more artifacts than those obtained at 0.8 GHz (Fig. 6).

C. Human Forearm

The obtained images for volunteer #1 and #4 are shown in Figs. 8 and 9, along with the respective MRI scan.

For the shape-and-location reconstruction, we presumed the dielectric properties of $\epsilon_r^{\text{muscle}} = 56 - j20$ and $\epsilon_r^{\text{bone}} = 13 - j3$ at 0.8 GHz. Similar to the leg experiment, the color plots of the real part of the permittivity is limited to 70, which is lower than that of the background fluid. Here, the imaging domain length is set to 10 cm.

VII. DISCUSSION AND CONCLUSION

In this study, we have utilized four different versions of the MR-GNI algorithm to enhance the imaging of biological objects using prior information. For the experimental part, we examined two different objects for imaging: *ex vivo* bovine legs and *in vivo* human forearms. For the bovine legs, we also presented directly measured values of the complex permittivity of the tissues in the imaging plane. For the human forearms, we presented the MRI scans of the arm.

The images of the skinless bovine leg are shown in Figs. 4 and 5 at the frequencies of 0.8 and 1.2 GHz, respectively. The 0.8-GHz dataset is a higher quality dataset compared to the 1.2-GHz data. This shows up as many oscillations and noise in the blindly reconstructed image at 1.2 GHz. We showed that providing prior information enhances the performance of the MR-GNI algorithm in all datasets. In the balanced shape-and-location reconstruction (the last row of the images), these oscillations were reduced. The different tissue types were clearly discernible in all of the enhanced images. The average reconstructed complex permittivity of the bone tissue is $22 - j6$ at 1.2 GHz, which is very close to the measured permittivity of $25 - j7$. Similar behavior is observed for the flexor tissue. Note that the matching fluid has penetrated into the skinless leg, which is visible in the results of Figs. 4 and 5.

The images of the leg with intact skin are shown in Figs. 6 and 7 at the frequencies of 0.8 and 1.2 GHz, respectively. In this case, the matching fluid did not penetrate into the leg, and thus, the quality of the images is higher compared to the previous case (without the skin). As shown in the first and fourth rows of Figs. 6 and 7, there are some oscillations and noise particularly in the imaginary part of the image. The first and fourth rows correspond to the blind inversion and shape-and-location inversion, respectively. The unwanted oscillations do not appear in the second and fifth rows in Figs. 6 and 7. These correspond to the balanced inversion and balanced shape-and-location inversion, respectively. Thus, the balancing enhancement is an important prior information for removing unwanted oscillations. In all the objects, the oscillations vanished after applying the balancing factor. For the bovine leg with skin, again the best image was obtained in the last row of the figures, which corresponds to the balanced shape-and-location reconstruction. The permittivity values of the bone and flexor tissue agree well with the measured values in Table II. Note that we used both types of bovine leg, with and without the skin, to experimentally test what effect the skin layer has on the imaging results. The exterior layer of most *in vivo* biomedical targets consists of a skin layer followed by a fat layer. The skin has a high-permittivity value, whereas the fat has a relatively low one. This sharp change at the interface of these two layers is a challenge for microwave image reconstruction. When using saltwater as a background, the skin layer seems to be less of a problem than

the fat layer. This can be seen from the images of the bovine legs, with and without skin, which contained little or no fat and are very well reconstructed.

The case is quite different for the human forearms where more fat is situated under the skin layer. From the five volunteers, we chose the two volunteers with the greatest difference in the thickness of the adipose layer under the skin layer. The reconstructed images for Volunteer #1 at 0.8 GHz, with a thin layer of adipose tissue, are shown in Fig. 8. The first row of the figure shows the blind inversion, which contains many oscillations and artifacts. The imaginary part is not reconstructed well with different tissues such as the bones and muscles not distinguishable. The second row in Fig. 8 shows the balancing enhancement. The oscillations have vanished, however, the bone and muscle tissues are still not clearly distinguishable. In the fourth row, using the shape-and-location reconstruction, as for the bovine legs, some oscillations appear, but the bone and muscle tissues are clearly distinguishable. Finally, by combining the balancing enhancement and shape-and-location enhancement, shown in the last row, the best image was produced. The results agree qualitatively with the MRI image.

Images for Volunteer #4 are shown in Fig. 9. The presence of a relatively thick adipose tissue is the main challenge and this shows up in the poorer quality of the images, as compared to images for Volunteer #1's, shown in Fig. 8. We have, however, presented these results to show that the images are still enhanced by utilizing the MR-GNI algorithm based on prior information. Again, the best image was obtained in the last row. The bone and muscle tissues are discernible, but the imaginary part does not distinguish different tissues.

In conclusion, we have collected experimental biomedical MWT data and showed the performance of three enhanced versions of the GNI inversion algorithm on inverting these data sets. These enhanced algorithms introduce some prior information into the MR-GNI algorithm, either: 1) the expected difference between the real and imaginary parts of the complex permittivity of the tissue; 2) the expected permittivity values of a number of tissues in the target; or 3) the combination of these two enhancements. We refer to these three enhancements as the balanced inversion, shape-and-location inversion, and balanced shape-and-location inversion, respectively. This approximate prior information can be obtained from the literature, or as was done in this study, it can be obtained directly from a preliminary quantitative blind inversion. Using both *ex vivo* experimental data, as well as *in-vivo* human forearm scattering data, we have shown that the resulting images can be significantly enhanced in this way.

ACKNOWLEDGMENT

The authors would like to thank Dr. C. Gilmore for providing them with the forearm data and the MRI images, as well as the Nano-Systems Fabrication Laboratory, University of Manitoba, for supplying the deionized water.

REFERENCES

[1] C. Eyraud, J. Geffrin, and A. Litman, "3D-aggregate quantitative imaging: Experimental results and polarization effects," *IEEE Trans. Antennas Propag.*, vol. 59, no. 4, pp. 1237–1244, Apr. 2011.

[2] A. Abubakar, T. Habashy, V. Druskin, L. Knizhnerman, and D. Alumbaugh, "2.5D forward and inverse modeling for interpreting low-frequency electromagnetic measurements," *Geophysics*, vol. 73, pp. F165–F177, 2008.

[3] T. Rubæk, O. Kim, and P. Meincke, "Computational validation of a 3-D microwave imaging system for breast-cancer screening," *IEEE Trans. Antennas Propag.*, vol. 57, no. 7, pp. 2105–2115, Jul. 2009.

[4] J. Stang, M. Haynes, P. Carson, and M. Moghaddam, "A preclinical system prototype for focused microwave thermal therapy of the breast," *IEEE Trans. Biomed. Eng.*, vol. 59, no. 9, pp. 2431–2438, Sep. 2012.

[5] J. Geffrin, P. Sabouroux, and C. Eyraud, "Free space experimental scattering database continuation: experimental setup and measurement precision," *Inverse Prob.*, vol. 21, pp. S117–S130, 2005.

[6] C. Gilmore, P. Mojabi, A. Zakaria, M. Ostadrahimi, C. Kaye, S. Noghianian, L. Shafai, S. Pistorius, and J. LoVetri, "A wideband microwave tomography system with a novel frequency selection procedure," *IEEE Trans. Biomed. Eng.*, vol. 57, no. 4, pp. 894–904, Apr. 2010.

[7] J. Bolomey and C. Pichot, "Microwave tomography: From theory to practical imaging systems," *Int. J. Imag. Syst. Technol.*, vol. 2, no. 2, pp. 144–156, 1990.

[8] M. Ostadrahimi, P. Mojabi, S. Noghianian, L. Shafai, S. Pistorius, and J. LoVetri, "A novel microwave tomography system based on the scattering probe technique," *IEEE Trans. Instrum. Meas.*, vol. 61, no. 2, pp. 379–390, Feb. 2012.

[9] A. R. Webb, *Introduction to Biomedical Imaging*. New York, NY, USA: Wiley, 2003.

[10] J. Jacobi, L. Larsen, and C. Hast, "Water-immersed microwave antennas and their application to microwave interrogation of biological targets," *IEEE Trans. Microw. Theory Techn.*, vol. MTT-27, no. 1, pp. 70–78, Jan. 1979.

[11] L. Larsen and J. Jacobi, "Microwave scattering parameter imagery of an isolated canine kidney," *Med. Phys.*, vol. 6, pp. 394–403, 1979.

[12] S. Semenov, J. Kellam, Y. Sizov, A. Nazarov, T. Williams, B. Nair, A. Pavlovsky, V. Posukh, and M. Quinn, "Microwave tomography of extremities: 1. Dedicated 2-D system and physiological signatures," *Phys. Med. Biol.*, vol. 56, pp. 2005–2017, 2011.

[13] S. Semenov, J. Kellam, B. Nair, T. Williams, M. Quinn, Y. Sizov, A. Nazarov, and A. Pavlovsky, "Microwave tomography of extremities: 2. Functional fused imaging of flow reduction and simulated compartment syndrome," *Phys. Med. Biol.*, vol. 56, pp. 2019–2030, 2011.

[14] N. Nikolova, "Microwave imaging for breast cancer," *IEEE Microw. Mag.*, vol. 12, no. 7, pp. 78–94, Dec. 2011.

[15] A. Hassan and M. El-Shenawee, "Review of electromagnetic techniques for breast cancer detection," *IEEE Rev. Biomed. Eng.*, vol. 4, pp. 103–118, 2011.

[16] P. M. Meaney, P. A. Kaufman, L. S. Muffly, M. Click, S. P. Poplack, W. A. Wells, G. N. Schwartz, R. M. di Florio-Alexander, T. D. Tosteson, Z. Li, S. D. Geimer, M. W. Fanning, T. Zhou, N. R. Epstein, and K. D. Paulsen, "Microwave imaging for neoadjuvant chemotherapy monitoring: Initial clinical experience," *Breast Cancer Res.*, vol. 15, no. 2, pp. 1–16, 2013.

[17] P. Meaney, D. Goodwin, A. Golnabi, T. Zhou, M. Pallone, S. Geimer, G. Burke, and K. Paulsen, "Clinical microwave tomographic imaging of the calcaneus: A first-in-human case study of two subjects," *IEEE Trans. Biomed. Eng.*, vol. 59, no. 12, pp. 3304–3313, Dec. 2012.

[18] L. Jofre, M. Hawley, A. Broquetas, E. de los Reyes, M. Ferrando, and A. Elias-Fuste, "Medical imaging with a microwave tomographic scanner," *IEEE Trans. Biomed. Eng.*, vol. 37, no. 3, pp. 303–312, Mar. 1990.

[19] P. Mojabi and J. LoVetri, "Enhancement of the Krylov subspace regularization for microwave biomedical imaging," *IEEE Trans. Med. Imag.*, vol. 28, no. 12, pp. 2015–2019, Dec. 2009.

[20] M. Pastorino, *Microwave Imaging*. New York, NY, USA: Wiley, 2010, vol. 208.

[21] S. Gabriel, R. Lau, and C. Gabriel, "The dielectric properties of biological tissues: II. Measurements in the frequency range 10 Hz to 20 GHz," *Phys. Med. Biol.*, vol. 41, pp. 2251–2269, 1996.

[22] M. Lazebnik *et al.*, "A large-scale study of the ultrawideband microwave dielectric properties of normal breast tissue obtained from reduction surgeries," *Phys. Med. Biol.*, vol. 52, pp. 6093–6115, 2007.

[23] R. Halter, T. Zhou, P. Meaney, A. Hartov, J. Richard, Jr., K. Rosenkranz, W. Wells, C. Kogel, A. Borsic, E. Rizzo, and K. Paulsen, "The correlation of *in vivo* and *ex vivo* tissue dielectric properties to validate electromagnetic breast imaging: Initial clinical experience," *Physiol. Meas.*, vol. 30, pp. S121–S136, 2009.

- [24] P. Mojabi and J. LoVetri, "A prescaled multiplicative regularized Gauss–Newton inversion," *IEEE Trans. Antennas Propag.*, vol. 59, no. 8, pp. 2954–2963, Aug. 2011.
- [25] P. Mojabi and J. LoVetri, "Microwave biomedical imaging using the multiplicative regularized Gauss–Newton inversion," *IEEE Antennas Wireless Propag. Lett.*, vol. 8, pp. 645–648, 2009.
- [26] C. Gilmore, A. Zakaria, J. LoVetri, and S. Pistorius, "A study of matching fluid loss in a biomedical microwave tomography system," *AAPM Med. Phys.*, vol. 40, no. 2, p. 023101 (1–14), 2013.
- [27] M. Ostadrahimi, P. Mojabi, C. Gilmore, A. Zakaria, S. Noghianian, S. Pistorius, and J. LoVetri, "Analysis of incident field modeling and incident/scattered field calibration techniques in microwave tomography," *IEEE Antennas Wireless Propag. Lett.*, vol. 10, pp. 900–903, 2011.
- [28] P. Mojabi, J. LoVetri, and L. Shafai, "A multiplicative regularized Gauss–Newton inversion for shape and location reconstruction," *IEEE Trans. Antennas Propag.*, vol. 59, no. 12, pp. 4790–4802, Dec. 2011.
- [29] K. D. Budras and R. E. Habel, *Bovine Anatomy*, 2nd ed. Hannover, Germany: Schlutersche, 2011.



Majid Ostadrahimi (S'09–M'12) received the B.Sc. degree in electrical engineering from the Sharif University of Technology, Tehran, Iran, in 2003, the M.Sc. degree (with highest distinction) from the Iran University of Science and Technology, Tehran, Iran, in 2006, respectively, and the Ph.D. degree in electrical and computer engineering from the University of Manitoba, Winnipeg, MB, Canada, in 2011.

He is currently a Post-Doctoral Fellow with the Department of Electrical and Computer Engineering, University of Manitoba. His main research interests lie in the areas of biomedical imaging, designing and developing MWT systems, near-field measurement, modulated scattering techniques, and inverse problems.

Dr. Ostadrahimi was the IEEE Winnipeg section treasurer (2010 and 2011).



Puyan Mojabi (M10) received the B.Sc. degree from the University of Tehran, Tehran, Iran, in 2002, the M.Sc. degree from the Iran University of Science and Technology, Tehran, Iran, in 2004, and the Ph.D. degree from the University of Manitoba, Winnipeg, MB, Canada, in 2010, all in electrical engineering.

He is currently an Assistant Professor with the Department of Electrical and Computer Engineering, University of Manitoba.



Amer Zakaria (S'05–M'13) received the B.Sc. degree in electrical engineering (*summa cum laude*) from the American University of Sharjah, Sharjah, United Arab Emirates, in 2005, the M.Sc. degree in microwave engineering (with high distinction) from the Munich University of Technology, Munich, Germany, in 2007, and the Ph.D. degree in electrical engineering from the University of Manitoba, Winnipeg, MB, Canada, in 2012.

In 2006 and 2007, he was with the RF Verification Department, Infineon Technologies, Munich, Germany. He is currently a Postdoctoral Fellow with the Department of Electrical and Computer Engineering, University of Manitoba, Winnipeg, MB, Canada. His research interests include inverse problems, computational electromagnetics, and the development of microwave imaging systems.



Joe LoVetri (S'84–M'84–SM'09) received the B.Sc. (with distinction) and M.Sc. degrees in electrical engineering from the University of Manitoba, Winnipeg, MB, Canada, in 1984 and 1987, respectively, the Ph.D. degree in electrical engineering from the University of Ottawa, Ottawa, ON, Canada, in 1991, and the M.A. degree in philosophy from the University of Manitoba, Winnipeg, MB, Canada, in 2006.

From 1984 to 1986, he was an Electromagnetic Interference (EMI)/Electromagnetic Compatibility (EMC) Engineer with the Sperry Defence Division, Winnipeg, MB, Canada. From 1986 to 1988, he was a TEMPEST Engineer with the Communications Security Establishment, Ottawa, ON, Canada. From 1988 to 1991, he was a Research Officer with the Institute for Information Technology, National Research Council of Canada. In 1991, his academic career began when he joined the Department of Electrical and Computer Engineering, The University of Western Ontario, where he remained until 1999. From 1997 to 1998, he spent a sabbatical year with the TNO Physics and Electronics Laboratory, The Hague, The Netherlands, during which time he was involved with time-domain computational methods and ground penetrating RADAR. In 1999, he joined the University of Manitoba, where he is currently Head of the Department of Electrical and Computer Engineering. From 2004 to 2009, he was the Associate Dean (Research and Graduate Programs) for the Faculty of Engineering. His main research interests lie in the areas of time-domain computational electromagnetics, modeling of electromagnetic compatibility problems, inverse problems, and biomedical imaging.



Lotfollah Shafai (S'67–M'69–SM'75–F'88–LF'07) received the B.Sc. degree from the University of Tehran, Tehran, Iran, in 1963, and the M.Sc. and Ph.D. degrees from the University of Toronto, Toronto, ON, Canada, in 1966 and 1969, respectively.

In November 1969, he joined the Department of Electrical and Computer Engineering, University of Manitoba, Winnipeg, MB, Canada, as a Lecturer, Assistant Professor (1970), Associate Professor (1973), Professor (1979), and Distinguished Professor (2002). His assistance to industry was instrumental in establishing an Industrial Research Chair in Applied Electromagnetics at the University of Manitoba in 1989, which he held until July 1994. In 1986, he established the symposium on Antenna Technology and Applied Electromagnetics, ANTEM, at the University of Manitoba, which has grown to be the premier Canadian conference in antenna technology and related topics.

Dr. Shafai is a Life Fellow of The Royal Society of Canada. In 2002, he was elected a Fellow of The Canadian Academy of Engineering and Distinguished Professor at The University of Manitoba. He holds a Canada Research Chair in Applied Electromagnetics and was the international chair of Commission B, International Union of Radio Science (URSI) (2005–2008). In 2009, he was elected a Fellow of the Engineering Institute of Canada. He was the recipient of numerous awards. In 1978, his contribution to the design of the first miniaturized satellite terminal for the Hermes satellite was selected as the Meritorious Industrial Design. In 1984, he received the Professional Engineers Merit Award. In 1985, he received "The Thinker" Award from the Canadian Patents and Development Corporation. From the University of Manitoba, he received Research Awards in 1983, 1987, and 1989, the Outreach Award in 1987, and the Sigma Xi Senior Scientist Award in 1989. In 1990, he received the Maxwell Premium Award from the IEE, London, U.K., and in 1993 and 1994, the Distinguished Achievement Awards from the Corporate Higher Education Forum. In 1998, he received the Winnipeg RH Institute Foundation Medal for Excellence in Research. In 1999 and 2000, he received the University of Manitoba Research Award. He was a recipient of the IEEE Third Millennium Medal in 2000. In 2003, he received an IEEE Canada Reginald A. Fessenden Medal and a Natural Sciences and Engineering Research Council (NSERC) Synergy Award. In 2009, he was the recipient of the IEEE Chen-To-Tai Distinguished Educator Award. In 2011, he received the Killam Prize in Engineering from The Canada Council.